Liquid Structure of Iron and Iron–Nitrogen–Carbon Alloys within the Cores of Small Terrestrial Bodies

Allison Pease[1], Jiachao Liu[1], Mingda Lv[1], Jack Piper[1], Yoshio Kono[2], and Susannah M. Dorfman[1]

[1]Department of Earth and Environmental Sciences, Michigan State University, East Lansing, Michigan, United States

[2]Department of Physics and Astronomy, Kwansei Gakuin University, Sanda, Japan.

Corresponding authors: Allison Pease (peaseall@msu.edu) and Susannah Dorfman (dorfman3@msu.edu)

Key Points:

- Our experiments and models show that Fe–Fe bonds in alloy melt are shorter with increasing pressure and longer with increasing N and C.
- Nitrogen or carbon contamination may result in an overestimation of Fe–Fe distances in experiments.
- Nitrogen and carbon increase the volume of liquid Fe alloy, contributing to density deficits in planetary cores.

Abstract

Nitrogen has been proposed to be stored within planetary cores, yet its effects on the structure and density of molten Fe-alloys have not been explored experimentally. Using energy-dispersive X-ray diffraction we determine the structure of Fe–N(–C) liquids at terrestrial planet core conditions (1–7 GPa and 1700–1900°C) within a Paris-Edinburgh press. Variation of N up to 7 wt.% and C up to 1.5 wt.% results in near-linear changes in Fe–Fe atom distances and structure factor with increasing light element content. We do not observe a significant pressure-driven structural transition in Fe–N(–C) liquids. We model the expansion of the Fe–Fe bonds using a modified Birch-Murnaghan equation of state. With this model, we demonstrate that N or C contamination could lead to an overestimation of the Fe–Fe distances of pure Fe. We observe that the incorporation of 1 wt.% N or C into Fe results in a change in Fe–Fe distances that is twice as significant as the effect of 1 GPa. By approximating the change in volume, we infer that N and C incorporated in liquid iron could contribute to the density deficit observed in the cores of terrestrial bodies.

Plain Language Summary

The iron-rich cores of planets and moons such as the Earth, Moon, Mercury, and Ganymede are partially to fully molten. Observations of molten cores, core densities, and magnetic fields indicate that light elements are alloyed with iron. The abundance and distribution of these light elements throughout the solar system is debated. In our experiments, we measure how varying amounts of nitrogen and carbon affect the structure of liquid iron. We modeled how the length and arrangement of chemical bonds changed for different pressures and compositions. Additionally, we developed a new model for the physical properties of pure liquid iron. This model can be used to help determine the abundance of light elements in the cores of rocky planets and moons.

1 Introduction

Geophysical observations of the Earth's core as well as the cores of small terrestrial bodies (e.g. the Moon, Mercury, and Ganymede) indicate they are composed of a molten Fe-alloy enriched in light elements (e.g. Birch, 1952; Margot et al., 2007; Schubert et al., 1996; Weber et al., 2011). Since Birch, 1952, the relatively low density of Earth's liquid outer core compared to that of pure Fe has been recognized to indicate the presence of up to 10 weight percent light elements that may include

S, C, Si, O, H, and N (Minobe et al., 2015; Poirier, 1994). Identities and amounts of light elements incorporated in Earth's core reflect accretion and differentiation processes and may impact elastic properties of the solid inner core (e.g. Chen et al. 2014; Minobe et al. 2015), the driving force for the magnetic dynamo (e.g. Landeau et al. 2022), and melting point and thermal state at the inner core boundary (e.g. Zhang et al. 2016). Likewise, for smaller planetary bodies which are constrained by relatively few observations, light elements are key to lowering the melting point of the core alloy and fueling the convection of molten cores. Evidence for partially or fully molten cores in terrestrial bodies includes current or ancient magnetic fields of the Moon (Laneuville et al., 2014), Mercury (Stevenson et al., 1983), and Ganymede (Kivelson et al., 1996), analysis of Apollo program seismic observations indicating discontinuous seismic wave velocity in the lunar core (Weber et al., 2011), Earth-based remote sensing and observations from Mariner 10 spacecraft of the large longitude librations of the Mercurian core (Margot et al., 2007), and Galileo spacecraft measurements of gravity of Ganymede (Schubert et al., 1996). Sulfur and carbon are predicted to be found within cores of small planets and moons (e.g. Harder & Schubert, 2001; Li et al., 2017; Steenstra et al., 2017), and they may have opposite and competitive behaviors during core formation (Tsuno et al., 2018). Nitrogen has been proposed to be stored together with carbon within planetary cores: Fe–N alloys are mutually soluble with Fe–C alloys as solids (Minobe et al., 2015) and as liquids (Jang et al., 2014; Speelmanns et al., 2018). Fe–N alloys have been observed in diamond inclusions proposed to originate from Earth's core-mantle boundary (Kaminsky & Wirth, 2017), and N could be sequestered into cores at reducing conditions (e.g. ΔIW -0.4 to 2.2) (Dalou et al., 2017; Grewal et al., 2021), could contribute to explaining observations of a superchondritic C/N ratio in the bulk silicate Earth (e.g. Gu et al., 2024; Huang et al., 2024; Marty, 2012). Matching the observed density of planetary cores remains a key constraint on composition, and geophysical properties of alloys at core conditions can provide a constraint on elemental abundance within planetary cores (e.g . Badro et al., 2014; Bajgain et al., 2021; Umemoto & Hirose, 2020)

Interpreting light element content of planetary cores is based on the behavior of pure metallic iron at extreme conditions, but previous studies have produced conflicting results about the structure, density, and compressibility of liquid Fe (e.g. Kono et al., 2015; Sanloup et al., 2000). A sharp pressure-induced transition in pure liquid Fe to a denser, more compressible, more highly

coordinated structure has been proposed based on X-ray diffraction observations (Kono et al., 2015; Sanloup et al., 2000) but is not universally observed. This change is observed at pressures near the bcc–fcc-liquid Fe triple point at 5 GPa (Sanloup et al., 2000) or at 6 GPa (Kono et al., 2015) and is inferred to represent a transition from bcc–like to fcc–like liquid structure. First-principles molecular dynamics and analysis of experimental results suggest this transition may instead correspond to a change in the connectivity of bonding coordination polyhedra from corner-sharing to more edge- and face-sharing (Lai et al., 2017). The structural transition may also correspond to a discontinuity in the slope of trends in the chemical partitioning of elements between liquid iron and silicate melt (Sanloup et al., 2011). However, in other experiments, no significant change is observed in the structure factor or pair distribution function near the bcc–fcc transition in the solid and up to 67 GPa (Shen et al., 2004). Experimental observations of pure iron reaching more extreme pressures may ignore bcc–like structural behavior in the limited pressure range near 1 bar and note that structural transitions between close-packed fcc–like and hcp–like liquid do not significantly affect density, representing the high pressure-temperature density of liquid iron with a single equation of state (Kuwayama et al., 2020). These studies also find that experimental and analytical details, such as pressure gradients and the angular range of diffraction data, may contribute to uncertainty and inconsistency between measurements of the density and compressibility of liquid iron.

Previous experimental and theoretical studies have documented composition-dependent structure changes in iron alloys, including the promotion or inhibition of pressure-induced structure changes. Molecular dynamics simulations find that elements in binary alloys with liquid iron fall into at least two categories of behavior based on substitution mechanisms: atoms with “Fe–like” atomic radii, Si and Ni, directly replace Fe in the liquid, while atoms with small atomic radii, e.g H, C, O, S, and N, are stored in quasi-interstitial sites (Posner & Steinle-Neumann, 2019). The sites are referred to as quasi-interstitial rather than interstitial as liquids do not have a crystalline structure. Alloys with light elements stored in quasi-interstitial sites (e.g. Fe–S, and Fe–C) have been observed to be highly compressible relative to liquid Fe (Sanloup et al., 2002; Terasaki et al., 2010), while alloys with direct substitution (e.g. Fe–Si) observed a negligible impact on compressibility (Sanloup et al., 2002, 2004). Further, experiments on alloys with small light elements observe different impacts on the liquid structure. Fe–Fe atomic distances in magnetic Fe–O alloys are longer (Morard et al., 2022), but when

modeled for a non-magnetic alloy the Fe–Fe atomic distances are comparable to pure Fe (Morard et al., 2022; Posner et al., 2017). Decreased Fe–Fe distances are observed for high concentrations > 30 atomic % of S in Fe–S, and Fe–C–S alloys (Zhao et al., 2023). However, the presence of a few atomic % S increases Fe–Fe distances in Fe–S alloys. Fe–S alloys have not been observed to undergo a pressure-induced structural change analogous to that in pure Fe, but both Fe–S and Fe–C–S alloys undergo a change in structure with composition (Kono et al., 2015; Morard et al., 2007; Sanloup et al., 2002; Shibazaki & Kono, 2018; Urakawa et al., 1998). Previous studies demonstrate that above ~30 atomic % S the Fe liquid structure is significantly perturbed by the quasi-interstitial inclusion of S atoms, resulting in a modified structure and a sharp decrease in Fe–Fe bond lengths (Zhao et al., 2023). In contrast, adding C increases nearest neighbor Fe–Fe distances, and Fe–C and Fe–Ni–C alloys were observed to undergo a pressure-induced structural change at ~5 GPa (Lai et al., 2017; Shibazaki et al., 2015). Although N is commonly stored with C, no previous experimental studies have investigated the impact of N on the density and liquid structure of molten Fe–alloys at relevant pressures and temperatures to terrestrial bodies. Laboratory experiments are needed to constrain N storage in terrestrial cores and interpret how the physical properties of Fe–N alloys impact observable geophysical features.

In this study, we systematically investigate the structure of liquid Fe–N and Fe–N(–C) alloys at pressure-temperature conditions relevant to the interior of the Moon, Ganymede, and the core-mantle boundary of Mercury.

2 Methods

Liquid structure experiments were prepared with six initial compositions ranging from pure Fe to 7.7 wt.% N (Table 1). The starting materials are ε-Fe_7N_3, γ′-Fe_4N, and Fe metal powders; nitride powders are from Kojundo Chemical Lab. Co. Ltd. The bulk composition of ε-Fe_7N_3 and γ′-Fe_4N used in this study are ~7.7 wt.% and ~5.3 wt.% N, respectively (Pease et al., 2024). The N ratio is lower than stoichiometry for γ′-Fe_4N due to the presence of up to 11 at.% metallic iron (Pease et al., 2024). Starting materials were mixed mechanically to obtain compositions with bulk N content intermediate between Fe_7N_3 and pure Fe.

Experiments were conducted within a Paris-Edinburgh press. Tungsten carbide anvils applied high pressures to a standard Paris-Edinburgh cell assembly (as in Kono et al. 2014). To prevent N contamination, between the BN capsule commonly used in previous experiments on Fe and Fe alloys (Kono et al., 2015; Shibazaki et al., 2015; Shibazaki & Kono, 2018), we used a MgO capsule (Figure 1). Pressure was determined based on the equation of state of MgO (Kono et al., 2010). High temperatures were generated by a resistive graphite heater and calibrated based on previous observations of the relationship between applied heater power and temperature (Kono et al. 2014).

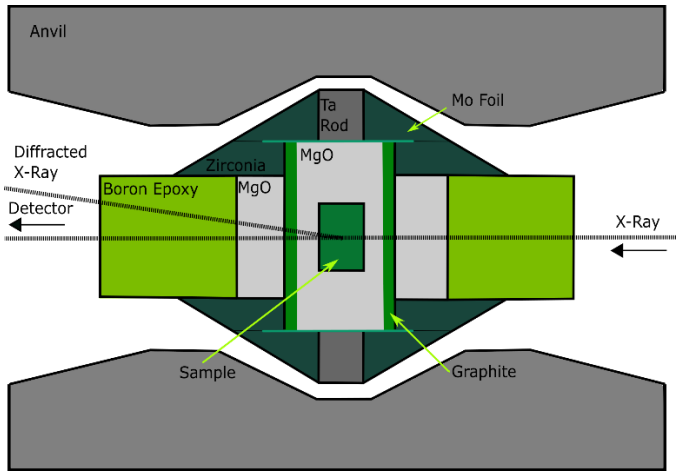

Figure 1: *Experimental setup for synchrotron X-ray measurements of the structure of Fe–N(–C) liquids at high pressures and temperatures in the Paris-Edinburgh press.*

X-ray radiography and energy dispersive X-ray diffraction (EDXD) were carried out at 16-BM-B, Advanced Photon Source, Argonne National Laboratory. Multi-angle EDXD measurements were collected if a single homogeneous liquid phase was observed based on the visual inspection of x-ray radiography images collected using a Prosilica GC1380H CCD camera (supplementary Figures s1 and s2). At low pressures and moderate temperatures, N may exsolve from Fe melt (Liu et al., 2019), so x-ray radiography was repeated after each EDXD measurement to confirm that the liquid was a homogenous single phase at ~1700–1900°C. High-pressure multiangle EDXD of Fe alloy liquid was collected using a Ge solid-state detector at 2-theta angles (4°, 5°, 7°, 9°, 12°, 16°, 22°, and 28°) (Figure 2). EDXD of the MgO capsule was obtained at a 2-theta angle of 15 degrees. The total exposure time/pressure step was ~3 hours. Data were analyzed using the aEDXD software package developed at 16-BM-B. The reduced pair distribution function, *G(r)*, was calculated from the Fourier

transform of the structure factor *S(Q)* with the maximum moment transfer Q up to 15. The multi-angle EDXD data were obtained for each liquid at ~1 GPa steps from minimum pressures of ~1–3 GPa to maximum pressures of ~5–7 GPa (Table 1). Temperatures were constant over all experiments except Run #2–17, for which temperature was increased from 1700 to 1825°C after the second data point was collected.

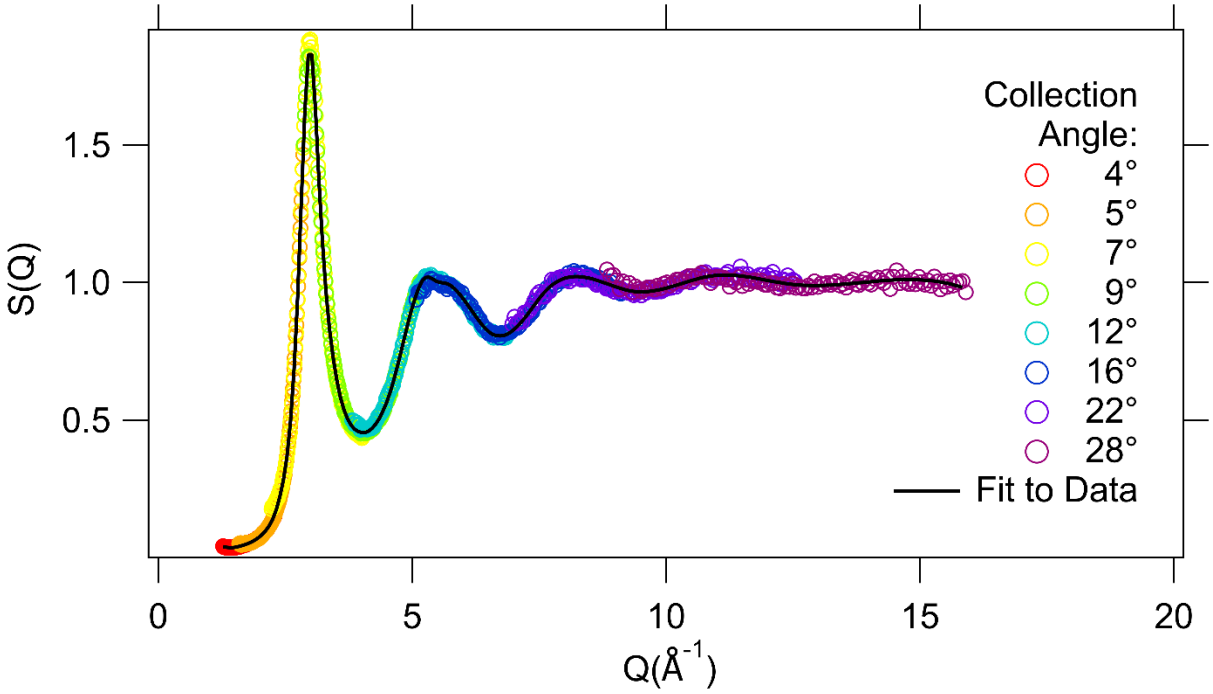

Figure 2: *Example of the structure factor [S(Q)] of Fe–N liquid obtained by processing multi-angle energy-dispersive X-ray diffraction data obtained at diffraction angles 4°–28° with aEDXD software. This data was collected for sample 2–16 with 1.4 wt.%N at 3 GPa and ~1700 °C.*

Compositions of recovered samples were analyzed using a Cameca SX-100 electron microprobe analyzer (EPMA) as described by Liu et al. (2019). To accurately detect light elements, N and C, we used Si_3N_4, Fe, and Fe_3C standards and coated samples and standards in Al. The detection limit is estimated to be ~500 ppm for both N and C. EPMA results indicate that the quenched melt composition is different from the bulk composition of the alloy as loaded: several samples exhibit a loss of multiple wt.% N during the experiment, and contamination with C up to 1.5 wt.% (Table 1). Loss of N from the sample is related to heating the sample at conditions where N solubility is low, allowing a separate N–rich fluid to advect and diffuse out through the capsule. As reported by Liu et

al. (2019), Fe–rich liquid may coexist with N–rich bubbles above the liquidus, and the solubility of N in Fe–rich liquid increases with pressure. X-radiography images for experiments reported in this work also indicate samples in experiments 1–16, 2–17, 3–16, and 12–17 separate into Fe–rich and N–rich fluid phases on first heating. The lower the pressure during the first heating, the greater the loss in N observed in the recovered sample (summary can be found in supplementary Figures s1 and s3). By proceeding to higher temperatures and pressures (and perhaps also by losing N from the system), each of these experiments reached conditions where x-radiography images indicate a single liquid phase. After this point, EDXD measurements were carried out. None of the samples exhibited a second episode of N exsolution. We do not expect that additional N was lost as the sample was compressed to its maximum pressure and then rapidly quenched, and previous studies have reported that more N can be dissolved in Fe and Fe–C melts as the pressure is increased (Liu et al., 2019; Speelmanns et al., 2018). Carbon may have entered the sample through a reaction with the graphite heater, as suggested by Liu et al., (2019). We observed C contamination within all experiments except run #2–16. We assume C was present in the sample upon first heating and remained constant throughout the experiment, however, because C ranged from 0.66–1.5% in most runs, given the constant possible C exchange we assume a ~1 wt.% uncertainty in the light element composition of the liquid. The final composition (reported in Table 1) is inferred to represent the composition of the liquid during EDXD measurements. The total N+C concentration in recovered Fe alloy samples ranges from ~1–8 wt.%.

Run #	Starting N (wt.%)	Starting C (wt.%)	Composition of Quenched Sample (wt.%)			
			Fe	N	C	Total
7–17**	0	0	100.0 (4)	BDL	1.2 (4)	100.9 (3)
2–17**	3	0	98.5 (9)	0.2 (4)	1.5 (6)	100.3 (7)
2–16*	1.5	0	97.7 (4)	1.4 (3)	BDL	99.1 (5)
3–16	5.3	0	96.3 (8)	3.2 (7)	0.66 (8)	100.1 (3)
1–16	7.7	0	96.3 (7)	2.8 (5)	0.66 (8)	99.8 (5)
12–17	7.7	0	92.8 (3)	6.9 (2)	0.77 (8)	100.5 (3)

Table 1: Summary of experimental run conditions. Initial compositions are determined from weight ratios and compositions of powder samples. Compositions of the recovered samples were determined by the electron microprobe analyzer (EPMA) and inferred to be the composition of each sample during liquid structure measurement by EDXD. BDL- stands for below detection limit. *Indicates the stability and composition of this experiment was previously documented in Liu et al., 2019. **Indicates the data was reprocessed from Liu et al., 2019. Please note run # 7–17 is referred to as 6–17 in Liu et al., 2019.

3 Results

EDXD data were used to calculate structure factor *S(Q)* and reduced pair distribution function *G(r)* for each composition and pressure. Given the low x-ray scattering factor of light elements N and C, the x-ray diffraction signal for Fe–N(–C) alloys is almost exclusively sensitive to the Fe atoms (e.g. Shibazaki et al. 2015). Figure 3 shows a characteristic plot of *S(Q)* and *G(r)* at each pressure step for experiment run # 2–16 where the composition was 1.4 wt.% N and 0 wt.% C. No new peaks or peak splitting were observed as the pressure increased (Figure 3).

Systematic differences in *S(Q)* and *G(r)* can be observed with increasing light element content at similar maximum pressures ~5 GPa (Figure 4). The first peak in *G(r)*, r_1, represents the average Fe–Fe bond length. The second peak in *G(r)*, r_2, represents multiple overlapping peaks corresponding to average distances to the next shell of Fe atoms in the liquid. An r_2 multiplet observed at high pressures and temperatures in previous studies (Sanloup et al., 2000; Shibazaki et al., 2015) has been interpreted to represent local bcc–like (high r) or fcc–like (low r) structures. More recently, this second peak has been identified by first-principles molecular dynamics calculations to be sensitive to the type of network formed by coordination polyhedra in iron–light element liquids, with corner-sharing between polyhedra corresponding to a peak at higher r_2 relative to edge- or face-sharing (Lai et al., 2017). The second peak in *S(Q)* appears as a doublet for compositions close to pure iron, with

a strong first peak and a weaker shoulder at higher Q. For the composition with the highest wt.% N, the doublet instead appears as a single peak at higher Q. The r_2 peak appears to be composed of two peaks at ~4.5 and 4.9 Å respectively, where their relative intensities are the greatest at 5–7 GPa depending on composition. At low wt.% N, the dominant peak is at ~4.5 Å; at high wt.% N, the dominant peak is at ~4.9 Å; and for run 2–17 with 1.7 wt.% N + C the intensities of the two peaks are ~equal. These observations could indicate that increasing incorporation of N promotes local bcc–like structure at high pressures or a higher proportion of corner-shared polyhedral groups of atoms in N–rich alloys.

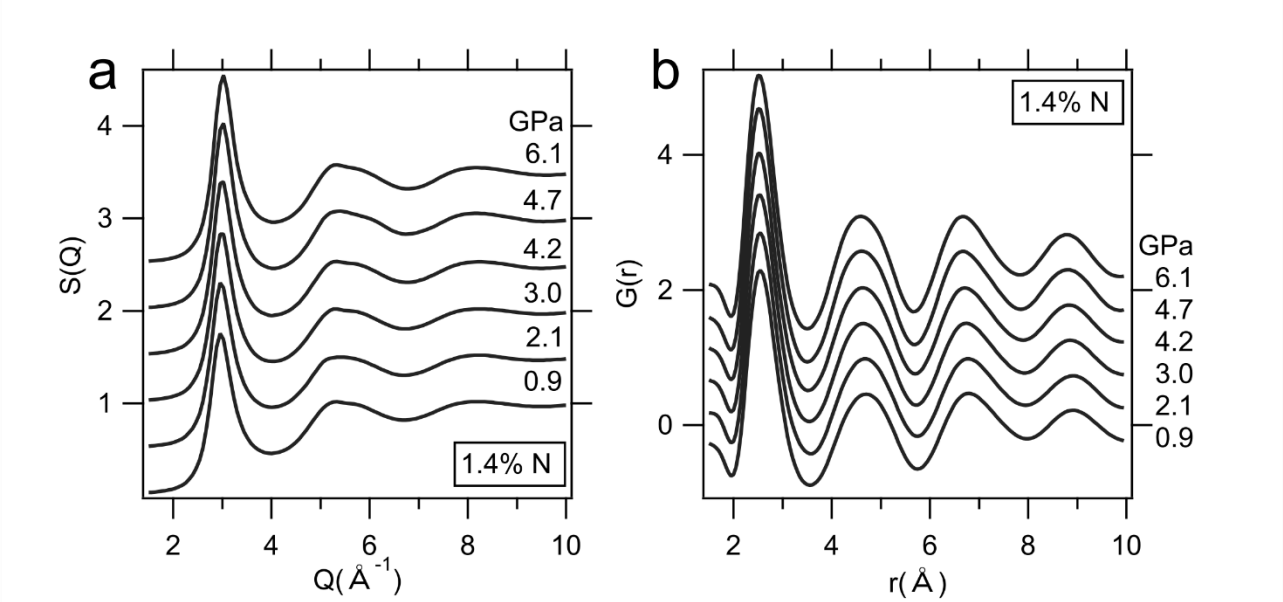

Figure 3: *(a) structure factor S(Q) and (b) reduced pair distribution function G(r) for all pressures from experiment run 2–16 (1.4 wt.% N). S(Q) and G(r) are displayed with a vertical offset of 0.5. G(r) plots for other compositions can be viewed in Figure S4 of the supplementary material.*

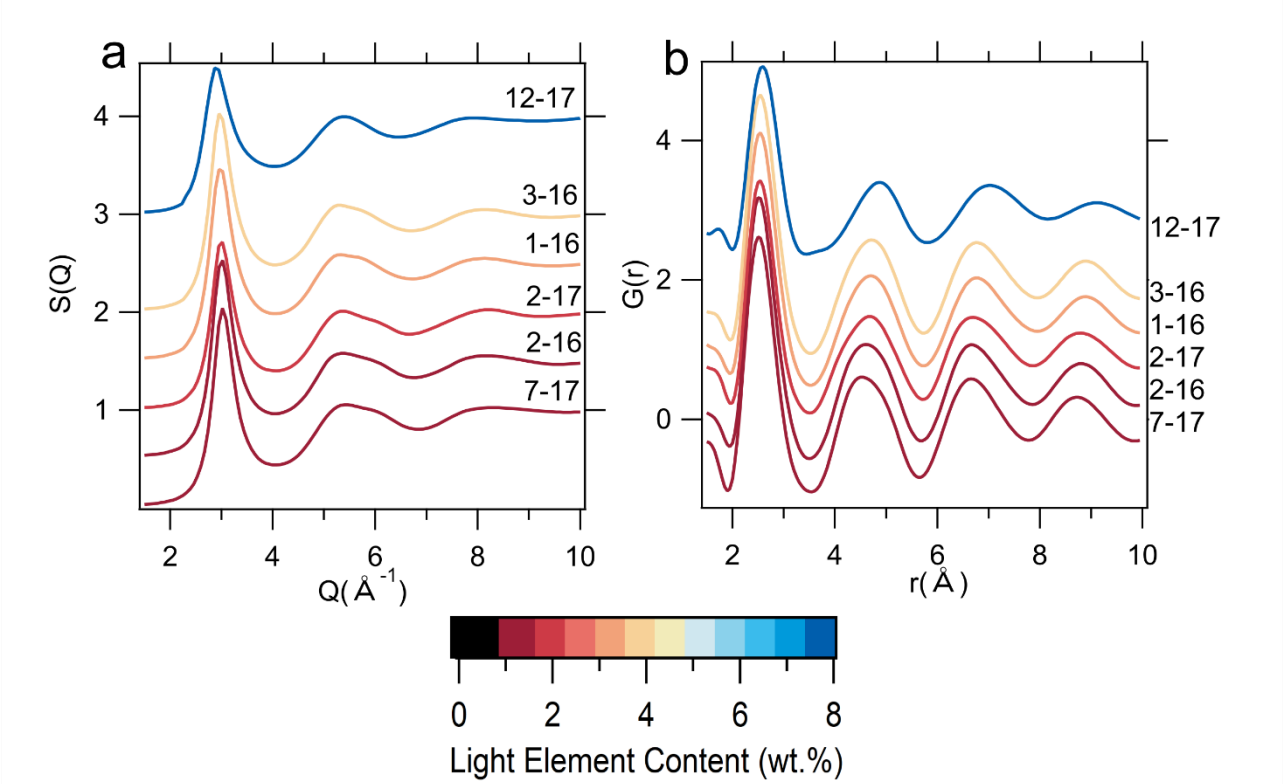

Figure 4: *(a) structure factor S(Q) and (b) reduced pair distribution function G(r) for all compositions around 5 GPa. Each run is denoted by its run # and vertically stacked for comparison. The light element abundance can be found in Table 1 or by referencing the color bar. S(Q) and G(r) are displayed with a vertical offset of 0.5. Run 12–17 is offset by an additional 0.5.*

To quantify trends in these spectra, Q_1, r_1, and r_2 were fit using an exponential Gaussian and a constant background. We were unable to consistently resolve a doublet fit to the r_2 multiplet (as in (Lai et al., 2017)). For each of our experiments, we observed that the r_1, peaks are centered at ~2.50–2.60 Å. For all compositions, we observe an increase in the first peak along *S(Q)*, Q_1, and a decrease in r_1 and r_2 with increasing pressure (Table 2 and Figure 5). In addition, we observe a decrease in Q_1 and an increase in r_1 and r_2 with increasing light element content (Figure 5). These observations are consistent with the compression of the Fe–Fe atomic distances under pressure and expansion with the incorporation of N and C.

234

Run #	N–rich fluid Exsolved?	Pressure (GPa)	Temperature (℃)	Q_1 ($Å^{-1}$)	r_1 (Å)	r_2 (Å)
7–17	No	1.2 (3)	1835 (50)	2.98 (1)	2.533 (5)	4.6642 (9)
		2.2 (3)	1828 (50)	3.00 (1)	2.528 (6)	4.633 (1)
		3.7 (3)	1826 (50)	3.01 (1)	2.519 (7)	4.592 (6)
		5.3 (3)	1833 (50)	3.03 (1)	2.516 (4)	4.57 (1)
		7.0 (3)	1831 (50)	3.04 (1)	2.502 (5)	4.546 (6)
2–17	Yes	3.0 (3)	1700 (50)	2.99 (2)	2.540 (6)	4.640 (2)
		3.3 (3)	1703 (50)	2.99 (1)	2.536 (4)	4.6568 (8)
		4.6 (3)	1826 (50)	2.99 (2)	2.545 (4)	4.658 (1)
		5.3 (3)	1825 (50)	3.00 (1)	2.537 (5)	4.6499 (1)
		6.1 (3)	1827 (50)	3.00 (2)	2.536 (5)	4.641 (4)
		7.3 (3)	1829 (50)	3.02 (2)	2.527 (5)	4.626 (5)
2–16	No	0.9 (3)	1726 (50)	2.97 (1)	2.548 (5)	4.693 (2)
		2.1 (3)	1731 (50)	2.97 (2)	2.546 (5)	4.6735 (5)
		3.0 (3)	1734 (50)	2.98 (1)	2.538 (4)	4.655 (1)
		4.2 (3)	1738 (50)	2.99 (2)	2.526 (8)	4.643 (1)
		4.7 (3)	1731 (50)	3.01 (1)	2.522 (8)	4.6205 (1)
		6.1 (3)	1727 (50)	3.02 (1)	2.522 (9)	4.612 (1)
3–16	Yes	1.2 (3)	1722 (50)	2.93 (1)	2.570 (7)	4.769 (2)
		2.0 (3)	1737 (50)	2.94 (2)	2.557 (5)	4.743 (2)
		2.9 (3)	1729 (50)	2.95 (1)	2.556 (4)	4.7311 (4)
		3.8 (3)	1736 (50)	2.96 (2)	2.546 (6)	4.726 (2)
		4.8 (3)	1733 (50)	2.97 (2)	2.545 (5)	4.692 (2)
		5.9 (3)	1729 (50)	2.98 (2)	2.541 (6)	4.673 (1)
		6.5 (3)	1733 (50)	2.98 (2)	2.538 (5)	4.666 (1)
1–16	Yes	1.8 (3)	1729 (50)	2.94 (2)	2.555 (4)	4.7509 (1)
		2.5 (3)	1729 (50)	2.96 (2)	2.554 (7)	4.738 (1)
		2.7 (3)	1729 (50)	2.95 (2)	2.552 (5)	4.725 (2)
		4.5 (3)	1740 (50)	2.98 (2)	2.543 (6)	4.688 (2)
		5.6 (3)	1732 (50)	2.98 (2)	2.541 (5)	4.675 (1)
12–17	Yes	3.2 (3)	1719 (50)	2.89 (2)	2.592 (2)	4.8599 (7)
		4.2 (3)	1728 (50)	2.90 (2)	2.585 (4)	4.8537 (1)
		5.0 (3)	1730 (50)	2.90 (1)	2.590 (2)	4.852 (6)

Table 2: Summary of experimental run conditions and fit values for Q_1, r_1, and r_2 based on an exponential modified Gaussian. The uncertainty for r_1 and r_2 is the standard deviation between a q_{max} of 15 and 13; reported values are fit to a q_{max} of 15. In Figure 5, the error bars assigned to r_2 are approximated to 0.01 to account for uncertainty pertaining to broadening. Choice of q_{max} has a more significant impact on r_1 than on r_2. The uncertainty for Q_1 is the standard deviation between *S(Q)* and the filtered *S(Q)*; the reported values are *S(Q)*.

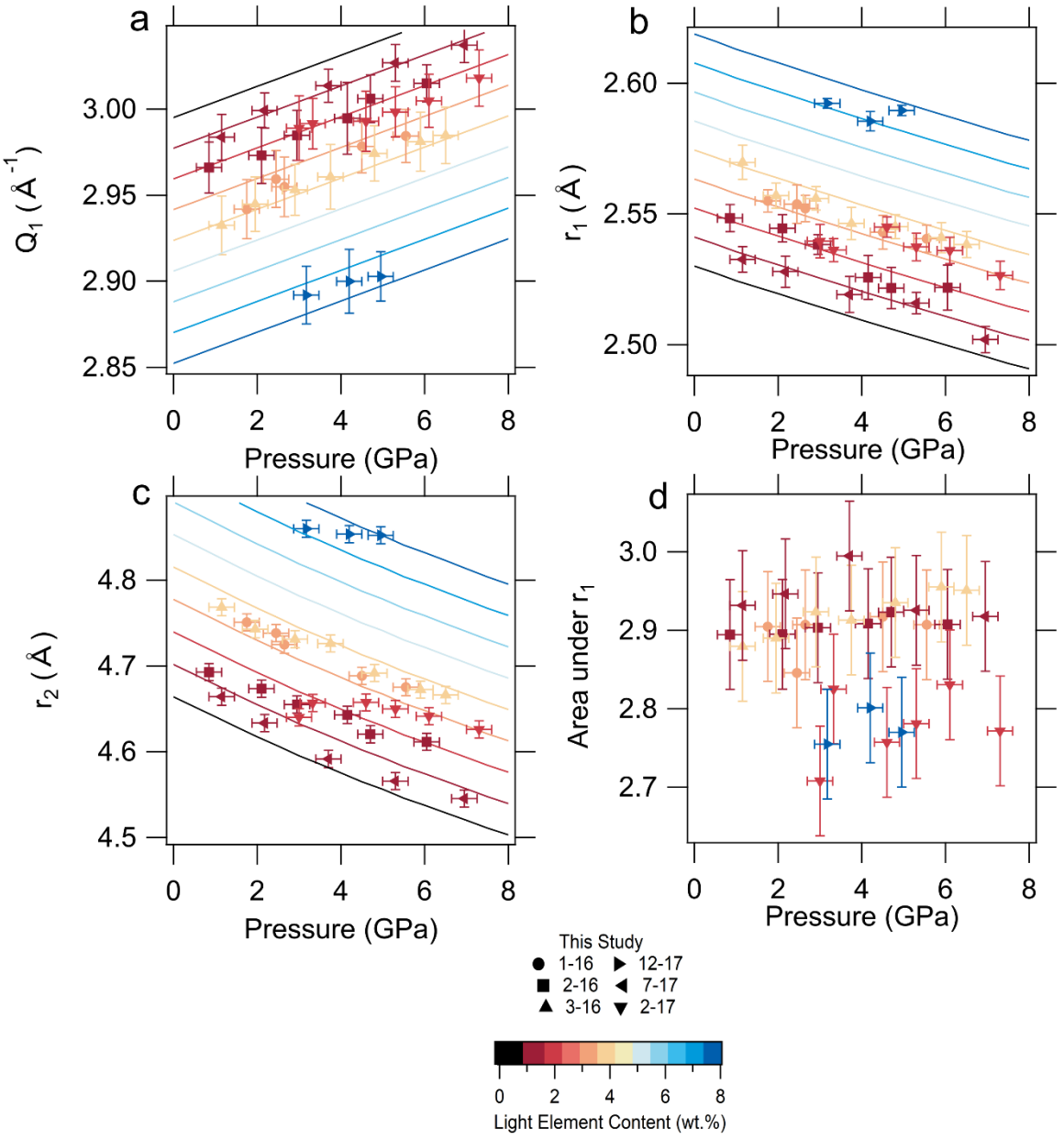

Figure 5: *Structure of Fe–N(–C) liquids at 1700–1900°C as a function of pressure and incorporation of N and C (summed as total light element content). (a) first structure factor peak (Q_1), (b) the first reduced pair distribution function peak (r_1), (c) the second reduced pair distribution function peak (r_2), and (d) the area under r_1, which depends on the average coordination of the liquid. Each run is indicated by a different symbol, and the light element content measured after recovery to ambient conditions is shown in colors indexed in the color bar (and in Table 1). Black lines represent pure Fe.*

Fits to a modified second-order Birch Murnaghan equation of state are used to model the effect of 0–8 wt.% light elements and pressure on the position of r_1, and r_2 (Equation 1), while a linear model is shown for Q_1 as a function of pressure and light element content (Equation 2).

Within the uncertainty and resolution of our data, we do not observe evidence for a pressure-induced structural change in any Fe–N(–C) liquid compositions. A structural change in molten pure Fe or Fe–alloy may be indicated by a discontinuous change (Lai et al., 2017; Sanloup et al., 2000) or a change in the slope of r_1, r_2 multiplet, and Q_1 with pressure (Lai et al., 2017; Shibazaki et al., 2015), as well as a corresponding change in the areas and shapes of peaks in *G(r)* due to changing bonding coordination (Cristiglio et al., 2009; Lai et al., 2017). Taken together, our Fe–Fe distances for Fe–N(–C) liquids can be described by a single modified Birch-Murnaghan (BM) equation of state for linear compressibility (Birch, 1952) with incompressibility constant with composition and a linear relationship between Fe–Fe distance, *r*, and total N + C light element content in wt.%, x:

Equation 1:

$$P(r,x) = \frac{3}{2} * k_0 * \left[\left(\frac{r_0 + x * \Delta r_0}{r}\right)^7 - \left(\frac{r_0 + x * \Delta r_0}{r}\right)^5\right] * \left[1 - \frac{3}{4} * \left(4 - k_0^p\right) * \left(\left(\frac{r_0 + x * \Delta r_0}{r}\right)^2 - 1\right)\right]$$

In this model, pressure (P(r,x)) varies as a function of *r* and *x* with fit parameters r_0, k_0, k_0^p, representing the linear compressibility for Fe–Fe atomic distances in pure Fe liquid (note that k_0 may not equal the bulk modulus of the material), and Δa_0 representing the effect of light element incorporation to expand Fe–Fe distances. In Figure 5 b and c, curves represent modeled linear compressibility at constant composition for pure metal up to 8 wt.% (N+C) (parameters reported in Table 3). We do not observe a fittable inflection point or systematic offset between experimental r_1 and r_2 at high pressure vs. low pressure which would indicate a discontinuous change in liquid structure. In addition, we find that Q_1 can be modeled with a linear response to both pressure and light element content, with three empirical fitting parameters *a*, *b*, and *c* from 1 to 8 wt.% (N+C) (Table 3):

Equation 2:

271 $$Q(P,x) = a + bP + cx$$

272

273 We also observe no systematic misfits relative to this linear model for structure factor that would
274 indicate a transition (Figure 5 a).

275 Finally, we calculated the area under r_1 as a proxy for the coordination number of the melt (e.g.
276 Cristiglio et al. 2009). The area of the r_1 peak is constant with pressure for all runs (Figure 5d),
277 although systematically lower for runs 2–17 and 12–17. If there is a pressure-induced structural
278 transition, we do not observe it having a statistically significant impact on the position of Q_1, r_1, and
279 r_2, for the Fe–N(–C) system relative to these models. The run with the highest concentration of N,
280 12–17 with ~8% light elements, is one of the low outlier runs in the area of r_1, which combined with
281 the higher r_2 peak may indicate lower coordination and more bcc–like or corner-shared structure at
282 high pressure relative to compositions close to pure Fe. Q_1, r_1, and r_2 can be modeled as varying
283 smoothly with pressure and linearly with N + C content.

284

Modified BM Fit parameters	r_0	k_0	k_0^p	Δa_0
r_1	2.530	155(18)	4	0.0111 (7)
r_2	4.665	61 (4)	4	0.037 (2)
Linear Fit Parameters	a	b	c	
Q_1	2.977 (3)	0.0090 (7)	-0.0179	

Table 3: Global fit parameters used in this study. r_0, K_0^p, and c were fixed, and all other variables were fit to the data. Modified BM fit parameters correspond to equation 1 and linear fit parameters correspond to equation 2.

285

4 Discussion

The Fe–Fe distances observed in this study for the experiment prepared by loading pure metallic Fe are systematically lower than previous studies (Figure 6). Unlike our study, previous studies of liquid structure of Fe (Kono et al., 2015; Sanloup et al., 2000; Shibazaki & Kono, 2018), Fe–C (Shibazaki et al., 2015; Shibazaki & Kono, 2018), and Fe–Ni–C (Lai et al., 2017) alloys report their composition as the composition that was loaded, do not report ex-situ composition analysis, and use a BN sample chamber. We expect that compositions as loaded do not accurately represent compositions of melt during experiments: we found that our experiment prepared as pure Fe contains 1.5 wt.% C upon recovery due to contamination by the graphite heater, and 2/3 recovered samples were measured with at least 1 wt.% difference in N, C, or both relative to the starting material. Moreover, we expect that BN capsules provide a source of N that will be soluble in Fe and Fe alloy melts at high pressures (e.g. Liu et al., 2019; Speelmanns et al., 2018). Nitrogen and/or carbon contamination may explain the higher r_1 observed in (Kono et al., 2015; Sanloup et al., 2000; Shibazaki & Kono, 2018) relative to the sample in this work with the lowest N and C content. Variability in light element contamination of Fe liquid during experiments through reaction with the enclosure may explain the wide range of reported r_1, ~6x the 1-σ error bar of the measurement. Kono et al., 2015 also note that the Re–W ball included in their study for viscosity measurements may have dissolved in their Fe melt, changing the composition. However, differences in analytical procedure, particularly the choice of q_{max}, may also result in systematic differences in the structure factor and pair distribution function. We find that running analysis with a lower q_{max} of 13, reducing the quality of the fit, systematically increases the positions of peaks in the pair distribution function *G(r)*. Our P–r–x model based on systematic composition variation and an N-free capsule provides an improved constraint on the physical properties of pure Fe liquid, which is the foundation for constraints on the light element content of small rocky bodies.

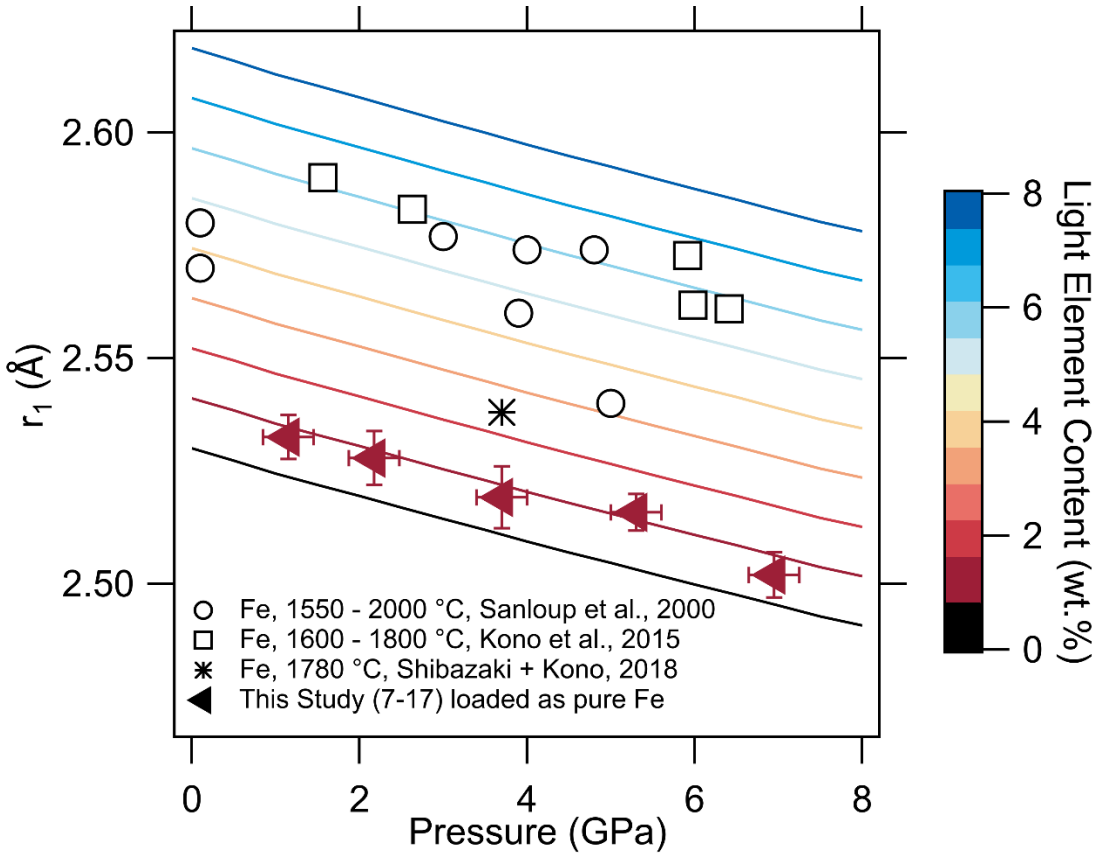

Figure 6: *Pressure dependence of the first reduced pair distribution function peak (r_1) between the global fit proposed in this study at (1700 – 1900 °C) and previous studies on Fe. Black lines and symbols represent pure Fe (as loaded). The temperature of previous studies ranges from ~1200–2000 °C. Unlike this study, previous studies report the composition as loaded rather than as measured ex-situ after the experiment.*

The expansion of atom-atom distances in Fe alloy liquid with the incorporation of N and C (Figure 5) appears similar to previous studies (Shibazaki & Kono, 2018). However, the comparison between our observations of the effects of N incorporation on Fe alloy liquid structure and previous studies of Fe–C or Fe–Ni–C systems (Figure 7) is complicated by differences in temperature, potential contamination, and differences in analytical methods. Qualitatively, our observations and previous studies of Fe–C and Fe–C–Ni systems observe that Q_1 decreases while r_1 and r_2 increase with increasing N or C content.

Our observations of the Fe–N(–C) system can be contrasted with qualitatively different behavior of Fe–S (Shibazaki & Kono, 2018) and Fe–S–C systems (Zhao et al., 2023). In S–bearing

systems, Fe–Fe distances are approximately unchanged with the incorporation of up to at least ~12 wt% S, above which concentration they decrease with increasing S (Figure 9). Reduction in r_1 for S-bearing Fe–alloys occurs at higher concentrations of light elements than compositions investigated in this study. For some previous studies, the magnitude of r_1 for C-bearing alloy liquid is similar to our model for the same wt.% N as reported wt.% C (Figure 7). Nitrogen and carbon incorporation result in a similar range in Q_1 and r_2 when compared to previous studies, but the absolute value of enriched light element abundances differs from previous studies (Lai et al., 2017; Shibazaki et al., 2015; Shibazaki & Kono, 2018). The difference in r_2 for the same amount of light elements by weight, ~8 wt.%, is lower for C than for N (Figure 8). The iso–nitrogen curves in Figures 5–7 were obtained by fitting data limited to a temperature range of ~1700–1900 °C, while the temperature range reported in previous studies spans ~1200–2000 °C. The thermal expansivity of the liquid is not constrained well enough to correct for temperature differences, but we can expect that increasing temperature would result in higher r_1.

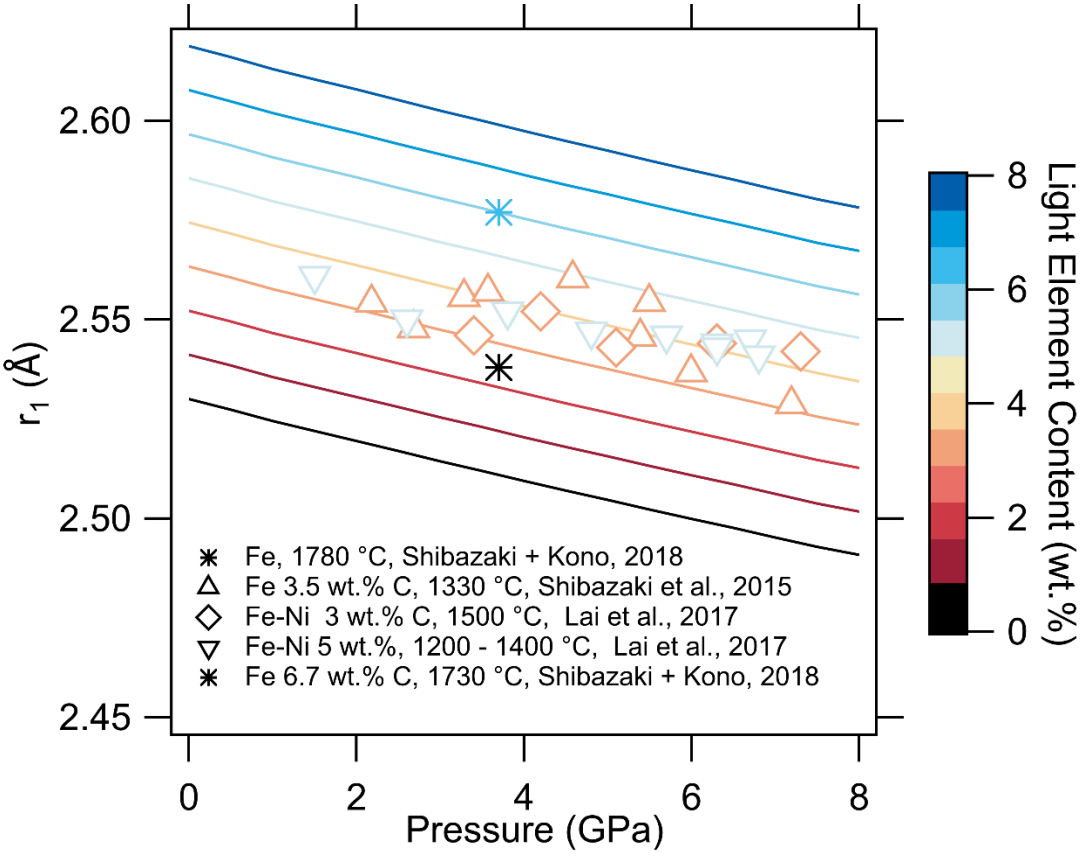

339

340 ***Figure 7:*** *Pressure dependence of the first reduced pair distribution function peak (r_1) between the*
341 *global fit proposed in this study at (1700 – 1900 °C) and previous studies. Black lines and symbols*
342 *represent pure Fe (as loaded). Unlike this study, previous studies report their composition as loaded*
343 *rather than as measured ex-situ after the experiment.*

344

345 While the results of Lai et al. 2017 for the Fe–Ni–C system indicate that pressure affects the
346 connectivity of bonding coordination in the melt, our results demonstrate a substantial effect of
347 composition on these structures. Lai et al. (2017) described this change by fitting the r_2 multiplet as
348 two peaks, r_{2s} at a smaller distance and r_{2m} at a longer distance, which correspond to mostly face-
349 shared coordination polyhedra and corner- and edge-shared polyhedra, respectively (Figure 8). Our
350 study and other previous studies fit the multiplet as a single peak (e.g (Shibazaki et al., 2015;
351 Shibazaki & Kono, 2018), but note that the asymmetry of the peak can change with pressure (e.g
352 (Lai et al., 2017)) and composition. When plotted relative to r_1 (Figure 8), we observe a sharp
353 increase in the average value of r_2 with increasing light element content, corresponding to a relative
354 increase in corner-shared polyhedral units. The most N-rich composition (run 12–17) exhibits a
355 similar average r_2 as what was reported for r_{2m} for Fe–Ni–C alloys (Lai et al., 2017). For C-free, N-
356 bearing samples (e.g. 2–16), r_2 is higher than in N-free, C-bearing samples (e.g. 7–17). The r_2 position
357 for the dominantly N-bearing alloy with ~8 wt.% N and C total is also substantially higher than the
358 alloy within similar total light element content dominated by C (Figure 8b) (Shibazaki & Kono, 2018).
359 The N-rich alloys may have a greater ratio of corner-shared polyhedral units relative to the C-rich
360 alloys. Alternatively, this may be interpreted as a bcc-like structure in the N-rich alloy (Sanloup et al.
361 2000).

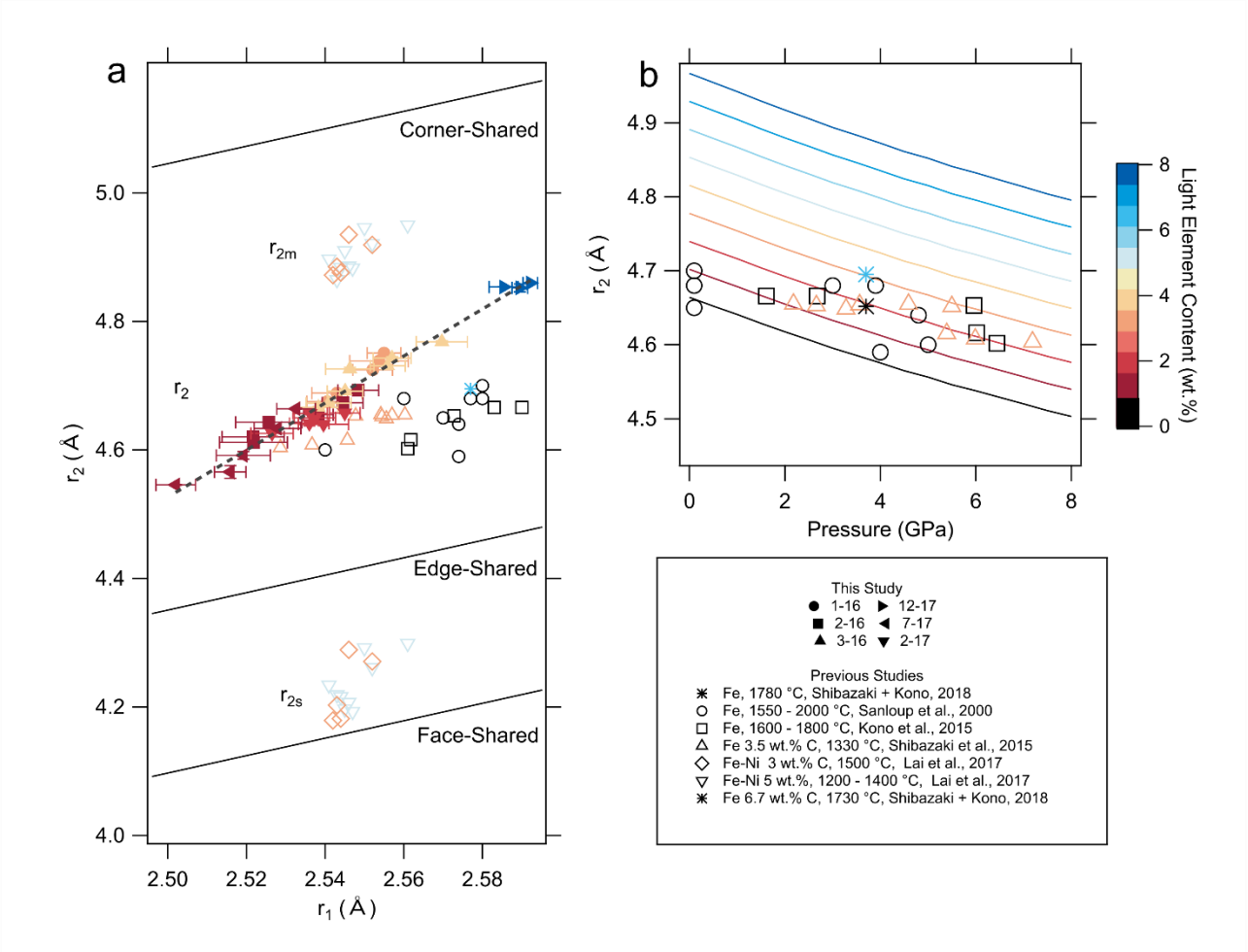

Figure 8: *Peak positions of r_2 with respect to r_1 (a) and pressure (b). Solid symbols are from this study, and open symbols are from previous studies* (Kono et al., 2015; Lai et al., 2017; Sanloup et al., 2000; Shibazaki et al., 2015; Shibazaki & Kono, 2018). *Color corresponds to the light element content (wt.%). (a) This study (fit with an* exponential modified Gaussian) *and previous studies (except Lai et al., 2017) fit and report one peak for r_2. Lai et al., (2017) fit two Gaussians to r_2 termed r_{2s} and r_{2m}. The black solid lines correspond to the predicted ideal r_2 for face, edge, and corner-shared motif connections based on molecular dynamics calculations published in Lai et al., (2017). The grey dashed line highlights the trend observed in this study for the Fe–N(–C) system. (b) Pressure dependence of the second reduced pair distribution function peak (r_2) between the global fit proposed in this study at 1700–1900 °C and previous studies. Unlike this study, previous studies report their composition as loaded rather than as measured ex-situ after the experiment.*

374 In contrast to this study, previous studies of Fe and Fe–C systems have interpreted liquid
375 structure observations to show a pressure-induced transition at ~5 GPa (Lai et al., 2017; Sanloup et
376 al., 2000; Shibazaki et al., 2015). A change in chemical partitioning of elements into liquid iron alloy
377 (Sanloup et al., 2011) has been suggested to be linked to the liquid structure transition. Sanloup et
378 al. (2000) documented the pressure and temperature impact on the liquid Fe structure up to 5 GPa,
379 and interpreted a decrease in r_1 and change in the shape of the r_2 peak from singlet to doublet as a
380 change from bcc structure to bcc + fcc. Lai et al., (2017) and Shibazaki et al., (2015) observed a
381 change in the slope of Q_1, r_1, and r_2 along with increased broadening in r_2 at higher pressures. Based
382 on their complementary molecular dynamics calculations, Lai et al., (2017), interpret their
383 observations to show a relative change in corner, edge, and face-sharing in polyhedral units of
384 atoms. Both Lai et al., (2017) and Shibazaki et al., (2015) observe consistent results for the behavior
385 of *r* and *Q*. In contrast, we don't see a correlated change in *r* and *Q* in Fe–N(–C) liquid with pressure.
386 A flat slope in Fe–Fe distances with pressure (as observed by Lai et al., 2017; Sanloup et al., 2000;
387 Shibazaki et al., 2015) relative to the compressibility of r_1 in Kono et al., 2015 and this study followed
388 by an increase in compressibility could also be explained by increasing N and C incorporation from
389 the reaction with a BN capsule and graphite heater. Given that the presence of C in the melt lowers
390 the solubility of N (Liu et al., 2019), we predict N-contamination could be the greatest in studies of
391 carbon-free compositions. Our data do not confirm a pressure-induced liquid structure transition,
392 although we acknowledge limited resolution in pressure that may hinder the identification of a
393 transition.

394

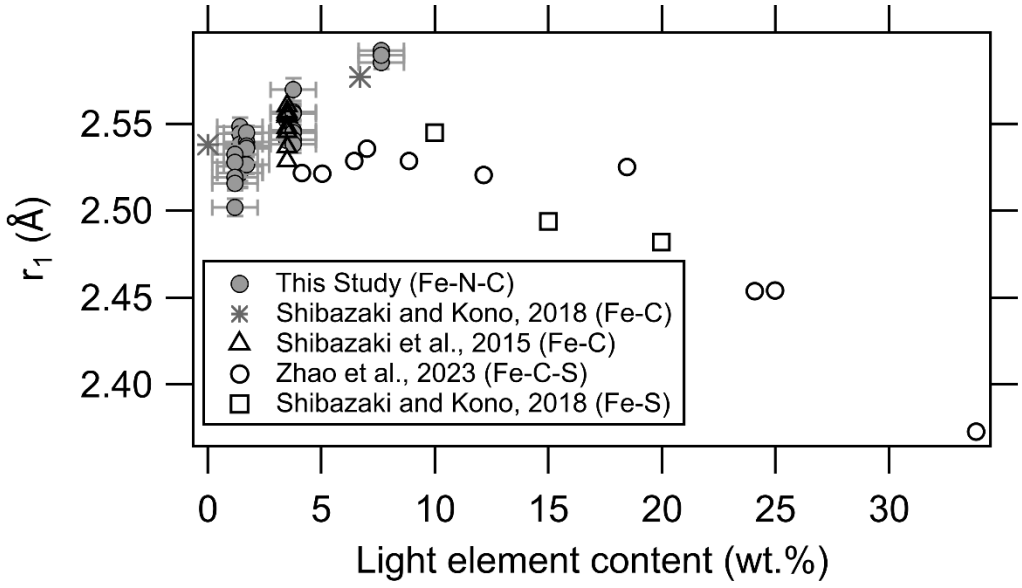

Figure 9: *Relationship between light element content at the nearest Fe–Fe bond (r_1). This study is represented by grey circles with the lower and upper bound of r_1 corresponding to observations at the maximum and minimum pressure, respectively. For previous studies, pressure ranges from 3–5 GPa* (Shibazaki & Kono, 2018)*, 2–7 GPa* (Shibazaki et al., 2015)*, and 1–5 GPa* (Zhao et al., 2023)*.*

The abundance of N and C in planetary cores inferred from remote sensing observations is constrained by the equation of state of the liquid alloy. Previous studies have demonstrated S and C increase the compressibility of liquid Fe (Sanloup et al., 2002; Terasaki et al., 2010), while Si has a negligible impact on Fe's compressibility (Sanloup et al., 2002, 2004). This is interpreted to be due to the quasi-interstitial incorporation of S and C vs. substitution mechanism for incorporation of Si (e.g. (Posner & Steinle-Neumann, 2019)). In this study, we fit pressure, composition, and r_1 or r_2 using a modified BM equation of state. Within this model, we do not change our value for incompressibility (K_0) as a function of composition, and observe a good fit to the data for light element abundance up to 7 wt.%. For run 12-17 with > 7 wt.% N and C we observe a less significant change in r_1 and r_2 with increasing pressure indicating the alloy could be more incompressible with increasing N and C content. This observation contradicts previous studies investigating the Fe–C system (e.g. Sanloup et al., 2002; Terasaki et al., 2010), and may be the result of data density in this study or N and C impacting Fe melts differently. Further, we observe that r_1 is more incompressible than r_2. In contrast, Morard et al. (2017) observed that the first coordination sphere in Fe–C liquid

414 was more compressible than the outer coordination spheres. This difference in Fe–Fe
415 compressibility for nearest and outer coordination spheres reflects differences in the incorporation
416 of N relative to C in the alloy.

417 The density of a molten Fe–N(–C) alloy is dependent on the abundance of light elements present
418 and the average atomic spacing in the liquid. The density of liquids can be obtained from the analysis
419 of diffraction data at low atomic spacings below the r_1 peak, provided that observations cover a wide
420 enough range of *Q* to converge(e.g. Morard et al., 2014). At low *r* values, we observe noise in G(r),
421 similar to previous measurements using the same method by Lai et al., (2017) but in contrast to
422 observations of Fe–C liquid based on monochromatic angle-dispersive synchrotron X-ray diffraction
423 (Morard et al., 2017). This noise may reflect a narrower range of Q_{max} constrained by the
424 experimental setup that prevents the extraction of density from the data. Morard et al., (2017)
425 determined the density of Fe with 1.8–3.7 wt.% C at 6 GPa and 1727°C to be 7,200 kg/m^3 (Morard
426 et al., 2017), and found that this density is sufficient to match the ~10% density deficit of Earth's
427 outer core relative to pure Fe. The uncertainty in density in these previous measurements is
428 significant: density may be underestimated for metallic liquids by up to 30% using x-ray diffraction
429 analysis with a hard sphere model (Ikuta et al., 2016). Although we do not apply this model to
430 measure density directly in this study, we can estimate a range of densities consistent with our
431 observed volumetric expansion and possible mechanisms for the incorporation of light elements. If
432 we assume volume per formula unit is directly related to the Fe–Fe atomic distance cubed, observed
433 expansion in Fe–Fe distance due to N and C would correspond to a volume change of 8–10 % when
434 8 wt.% light elements are present (supplementary Figure S5). If N and C are stored quasi-interstitially
435 (e.g. Posner & Steinle-Neumann, 2019), then the effective mass of the Fe-alloy would be greater
436 than the mass of pure Fe by ~8%. This suggests a bound on the density decrease for purely quasi-
437 interstitial N and C of ~0–2%. Either the effect of N and C on density decrease relative to pure Fe is
438 lower than previously reported, allowing for a higher concentration of N and C in planetary cores
439 than expected, or some N and C incorporation by substitution would be consistent with our
440 observations.

441 The composition of Earth's outer core is constrained using a combination of experimental
442 analogs, geophysical observations, and cosmochemical and geochemical calculations (e.g. Hirose et

al., 2021; Trønnes et al., 2019). The light element components in Earth's outer core have been estimated to include <1 wt.% of N and C combined; with up to 0.2 to 0.5 wt.% C (Fischer et al., 2020; Gu et al., 2024; Hirose et al., 2021) and up to 0.03 to 2 wt.% N (Bajgain et al., 2019; Gu et al., 2024). Like Earth, other terrestrial bodies (e.g. the Moon, Mercury, and Ganymede) are predicted to have partially or fully molten cores (e.g. Kivelson et al., 1996; Laneuville et al., 2014; Margot et al., 2007; Schubert et al., 1996; Stevenson et al., 1983; Weber et al., 2011). The distribution of light elements in the cores of these smaller bodies is expected to differ from Earth due to differences in compositions of material accreted at different distances from the sun and the pressure-temperature-oxygen fugacity conditions during differentiation (e.g. Grewal et al., 2019; Rubie et al., 2015). Bodies close to the sun are predicted to be enriched in Si: Mercury's core has been proposed to contain ~15 wt.% Si (Trønnes et al., 2019). The cores of bodies further from the sun are predicted to be relatively enriched in S: < 6wt.% sulfur in the lunar core (Weber et al., 2011) and ~10-20 wt.% in the Martian core (Brennan et al., 2020; Gendre et al., 2022). The solubility of C in Fe-alloys decreases with increasing S content (Tsuno et al., 2018), indicating that the abundance of C may be linked to concentration of S. The concentration of C in the Martian core may range from ~10ppm – 3.5 wt.% C (Tsuno et al., 2018), while the core of the Moon may range from 0.6–4.8 wt.% C (Steenstra et al., 2017). These estimates demonstrate the significant uncertainty and range in expected terrestrial planet and moon core compositions. Relatively few studies have estimated the abundance of N and C in terrestrial bodies; our model provides systematic constraints on effects of < 8wt.% N and C on volume of Fe alloy that support future studies of planetary core compositions.

5 Conclusions

The abundance of N and C in planetary cores is linked to the pressure-temperature-composition range during core formation. When N is incorporated into a molten Fe-alloy, it decreases the density and increases the distance between the nearest Fe–Fe atoms. The effects of N and C on the length of the nearest Fe–Fe atoms and the structure factor are similar, making them difficult to distinguish. However, N may have a stronger effect on the connectivity of polyhedral coordination units in the melt compared to C. Our results provide an equation of state for the liquid structure as a function of pressure and light element content. Given the similar behavior between N and C, we suggest that

N is hosted in the liquid structure by the same mechanism, quasi-interstitial incorporation, that is proposed for C.

The pressure effect on Fe–Fe atom distances and structure factor for all Fe–N(–C) alloys in this study is smooth within uncertainty up to 7 GPa, in contrast with previous studies of Fe, Fe–C, and Fe–S systems that observed a structural transition (Kono et al., 2015; Sanloup et al., 2000; Shibazaki et al., 2015; Zhao et al., 2023) with increasing pressure or light element content. A difference of approximately 2 wt.% N and/or C have the same effect as the observed change in the nearest Fe–Fe distance proposed for a liquid structure transition between 3–5 GPa. The abundance of light elements has a relatively stronger impact on the Fe–Fe bond distance and density compared to the structure transition inferred in previous studies. Further, our new data indicates that previous studies could have overestimated Fe–Fe distances. We find that N and C systematically impact the melt structure of Fe-alloys. There is no discontinuous change in Fe–Fe bonds or volume, so we propose that a pressure-composition equation of state can be used to predict the liquid structure. This systematic change in volume with pressure and temperature can be used to understand the density deficit in planetary cores.

Acknowledgments

We would like to acknowledge the assistance provided by O. Neill and J. Li in preparing the samples and standards for electron microprobe analysis at the University of Michigan. We would also like to recognize the assistance and user support provided by T. Estmond and R. Hrubiak regarding the aEDXD software. Part of this work was performed at HPCAT (Sector 16), Advanced Photon Source (APS), Argonne National Laboratory. HPCAT operations are supported by DOE-NNSA's Office of Experimental Sciences. The Advanced Photon Source, a U.S. Department of Energy (DOE) Office of Science User Facility operated for the DOE Office of Science by Argonne National Laboratory under Contract No. DE-AC02-06CH11357. A. Pease and beamline facility access was supported by the US Department of Energy, National Nuclear Security Administration, through the Chicago/DOE Alliance Center (DE- NA0003975). S. Dorfman, M. Lv, J. Piper acknowledge support from NSF EAR-1751664.

Open Research:

In this work, calculations were performed using aEDXD software (this software can be accessed at https://github.com/hp-edxd/hp-edxd), the processed energy dispersive X-ray diffraction data (S(Q) and G(r)) from this study can be found in Pease et al., 2024. The composition data can be found within supplementary dataset 1 (ds01) and a summary of the experiment conditions/MgO peak locations is in supplementary dataset 2 (ds02).

References

Badro, J., Côté, A. S., & Brodholt, J. P. (2014). A seismologically consistent compositional model of Earth's core. *Proceedings of the National Academy of Sciences*, *111*(21), 7542–7545. https://doi.org/10.1073/pnas.1316708111

Bajgain, S. K., Mookherjee, M., Dasgupta, R., Ghosh, D. B., & Karki, B. B. (2019). Nitrogen Content in the Earth's Outer Core. *Geophysical Research Letters*, *46*(1), 89–98. https://doi.org/https://doi.org/10.1029/2018GL080555

Bajgain, S. K., Mookherjee, M., & Dasgupta, R. (2021). Earth's core could be the largest terrestrial carbon reservoir. *Communications Earth & Environment*, *2*(1), 165. https://doi.org/10.1038/s43247-021-00222-7

Birch, F. (1952). Elasticity and constitution of the Earth's interior. *Journal of Geophysical Research (1896-1977)*, *57*(2), 227–286. https://doi.org/https://doi.org/10.1029/JZ057i002p00227

Brennan, M. C., Fischer, R. A., & Irving, J. C. E. (2020). Core formation and geophysical properties of Mars. *Earth and Planetary Science Letters*, *530*, 115923. https://doi.org/https://doi.org/10.1016/j.epsl.2019.115923

Chen, B., Li, Z., Zhang, D., Liu, J., Hu, M. Y., Zhao, J., et al. (2014). Hidden carbon in Earth's inner core revealed by shear softening in dense Fe7C3. *Proceedings of the National Academy of Sciences*, *111*(50), 17755–17758. https://doi.org/10.1073/pnas.1411154111

Cristiglio, V., Cuello, G. J., Piarristeguy, A. A., & Pradel, A. (2009). The coordination number calculation from total structure factor measurements. *Journal of Non-Crystalline Solids*, *355*(37), 1811–1814. https://doi.org/https://doi.org/10.1016/j.jnoncrysol.2008.12.027

Dalou, C., Hirschmann, M. M., von der Handt, A., Mosenfelder, J., & Armstrong, L. S. (2017). Nitrogen and carbon fractionation during core–mantle differentiation at shallow depth. *Earth and Planetary Science Letters*, *458*, 141–151. https://doi.org/https://doi.org/10.1016/j.epsl.2016.10.026

Fischer, R. A., Cottrell, E., Hauri, E., Lee, K. K. M., & Le Voyer, M. (2020). The carbon content of Earth and its core. *Proceedings of the National Academy of Sciences*, *117*(16), 8743–8749. https://doi.org/10.1073/pnas.1919930117

Gendre, H., Badro, J., Wehr, N., & Borensztajn, S. (2022). Martian core composition from experimental high-pressure metal-silicate phase equilibria. *Geochemical Perspectives Letters*,

21, 42–46. https://doi.org/https://doi.org/10.7185/geochemlet.2216

Grewal, D. S., Dasgupta, R., Sun, C., Tsuno, K., & Costin, G. (2019). Delivery of carbon, nitrogen, and sulfur to the silicate Earth by a giant impact. *Science Advances*, *5*(1), eaau3669. https://doi.org/10.1126/sciadv.aau3669

Grewal, D. S., Dasgupta, R., Hough, T., & Farnell, A. (2021). Rates of protoplanetary accretion and differentiation set nitrogen budget of rocky planets. *Nature Geoscience*, *14*(6), 369–376. https://doi.org/10.1038/s41561-021-00733-0

Gu, J. T., Peng, B., Ji, X., Zhang, J., Yang, H., Hoyos, S., et al. (2024). Composition of Earth's initial atmosphere and fate of accreted volatiles set by core formation and magma ocean redox evolution. *Earth and Planetary Science Letters*, *629*, 118618. https://doi.org/https://doi.org/10.1016/j.epsl.2024.118618

Harder, H., & Schubert, G. (2001). Sulfur in Mercury's Core? *Icarus*, *151*(1), 118–122. https://doi.org/https://doi.org/10.1006/icar.2001.6586

Hirose, K., Wood, B., & Vočadlo, L. (2021). Light elements in the Earth's core. *Nature Reviews Earth & Environment*, *2*(9), 645–658. https://doi.org/10.1038/s43017-021-00203-6

Huang, D., Siebert, J., Sossi, P., Kubik, E., Avice, G., & Murakami, M. (2024). Nitrogen sequestration in the core at megabar pressure and implications for terrestrial accretion. *Geochimica et Cosmochimica Acta*, *376*, 100–112. https://doi.org/https://doi.org/10.1016/j.gca.2024.05.010

Ikuta, D., Kono, Y., & Shen, G. (2016). Structural analysis of liquid aluminum at high pressure and high temperature using the hard sphere model. *Journal of Applied Physics*, *120*(13), 135901. https://doi.org/10.1063/1.4963278

Jang, J.-M., Seo, S.-H., Jiang, M., Paek, M.-K., Wang, X., & Pak, J.-J. (2014). Nitrogen Solubility in Liquid Fe–C Alloys. *ISIJ International*, *54*(1), 32–36. https://doi.org/10.2355/isijinternational.54.32

Kaminsky, F., & Wirth, R. (2017). Nitrides and carbonitrides from the lowermost mantle and their importance in the search for Earth's "lost" nitrogen. *American Mineralogist*, *102*(8), 1667–1676. https://doi.org/10.2138/am-2017-6101

Kivelson, M. G., Khurana, K. K., Russell, C. T., Walker, R. J., Warnecke, J., Coroniti, F. V, et al. (1996). Discovery of Ganymede's magnetic field by the Galileo spacecraft. *Nature*, *384*(6609), 537–541. https://doi.org/10.1038/384537a0

Kono, Y., Irifune, T., Higo, Y., Inoue, T., & Barnhoorn, A. (2010). PVT relation of MgO derived by simultaneous elastic wave velocity and in situ X-ray measurements: A new pressure scale for the mantle transition region. *Physics of the Earth and Planetary Interiors*, *183*(1), 196–211. https://doi.org/https://doi.org/10.1016/j.pepi.2010.03.010

Kono, Y., Park, C., Kenney-Benson, C., Shen, G., & Wang, Y. (2014). Toward comprehensive studies of liquids at high pressures and high temperatures: Combined structure, elastic wave velocity, and viscosity measurements in the Paris–Edinburgh cell. *Physics of the Earth and Planetary*

Interiors, *228*, 269–280. https://doi.org/https://doi.org/10.1016/j.pepi.2013.09.006

Kono, Y., Kenney-Benson, C., Shibazaki, Y., Park, C., Shen, G., & Wang, Y. (2015). High-pressure viscosity of liquid Fe and FeS revisited by falling sphere viscometry using ultrafast X-ray imaging. *Physics of the Earth and Planetary Interiors*, *241*, 57–64. https://doi.org/https://doi.org/10.1016/j.pepi.2015.02.006

Kuwayama, Y., Morard, G., Nakajima, Y., Hirose, K., Baron, A. Q. R., Kawaguchi, S. I., et al. (2020). Equation of State of Liquid Iron under Extreme Conditions. *Physical Review Letters*, *124*(16), 165701. https://doi.org/10.1103/PhysRevLett.124.165701

Lai, X., Chen, B., Wang, J., Kono, Y., & Zhu, F. (2017). Polyamorphic Transformations in Fe-Ni-C Liquids: Implications for Chemical Evolution of Terrestrial Planets. *Journal of Geophysical Research: Solid Earth*, *122*(12), 9745–9754. https://doi.org/https://doi.org/10.1002/2017JB014835

Landeau, M., Fournier, A., Nataf, H.-C., Cébron, D., & Schaeffer, N. (2022). Sustaining Earth's magnetic dynamo. *Nature Reviews Earth & Environment*, *3*(4), 255–269. https://doi.org/10.1038/s43017-022-00264-1

Laneuville, M., Wieczorek, M. A., Breuer, D., Aubert, J., Morard, G., & Rückriemen, T. (2014). A long-lived lunar dynamo powered by core crystallization. *Earth and Planetary Science Letters*, *401*, 251–260. https://doi.org/https://doi.org/10.1016/j.epsl.2014.05.057

Li, Y., Dasgupta, R., & Tsuno, K. (2017). Carbon contents in reduced basalts at graphite saturation: Implications for the degassing of Mars, Mercury, and the Moon. *Journal of Geophysical Research: Planets*, *122*(6), 1300–1320. https://doi.org/https://doi.org/10.1002/2017JE005289

Liu, J., Dorfman, S. M., Lv, M., Li, J., Zhu, F., & Kono, Y. (2019). Loss of immiscible nitrogen from metallic melt explains Earth's missing nitrogen. *Geochemical Perspectives Letters*, *11*, 18–22. https://doi.org/https://doi.org/10.7185/geochemlet.1919

Margot, J. L., Peale, S. J., Jurgens, R. F., Slade, M. A., & Holin, I. V. (2007). Large Longitude Libration of Mercury Reveals a Molten Core. *Science*, *316*(5825), 710–714. https://doi.org/10.1126/science.1140514

Marty, B. (2012). The origins and concentrations of water, carbon, nitrogen and noble gases on Earth. *Earth and Planetary Science Letters*, *313–314*, 56–66. https://doi.org/https://doi.org/10.1016/j.epsl.2011.10.040

Minobe, S., Nakajima, Y., Hirose, K., & Ohishi, Y. (2015). Stability and compressibility of a new iron-nitride β-Fe7N3 to core pressures. *Geophysical Research Letters*, *42*(13), 5206–5211. https://doi.org/https://doi.org/10.1002/2015GL064496

Morard, G, Sanloup, C., Fiquet, G., Mezouar, M., Rey, N., Poloni, R., & Beck, P. (2007). Structure of eutectic Fe–FeS melts to pressures up to 17 GPa: Implications for planetary cores. *Earth and Planetary Science Letters*, *263*(1), 128–139. https://doi.org/https://doi.org/10.1016/j.epsl.2007.09.009

Morard, G, Garbarino, G., Antonangeli, D., Andrault, D., Guignot, N., Siebert, J., et al. (2014). Density measurements and structural properties of liquid and amorphous metals under high pressure. *High Pressure Research*, *34*(1), 9–21. https://doi.org/10.1080/08957959.2013.860137

Morard, G, Nakajima, Y., Andrault, D., Antonangeli, D., Auzende, A. L., Boulard, E., et al. (2017). Structure and Density of Fe-C Liquid Alloys Under High Pressure. *Journal of Geophysical Research: Solid Earth*, *122*(10), 7813–7823. https://doi.org/https://doi.org/10.1002/2017JB014779

Morard, Guillaume, Antonangeli, D., Bouchet, J., Rivoldini, A., Boccato, S., Miozzi, F., et al. (2022). Structural and Electronic Transitions in Liquid FeO Under High Pressure. *Journal of Geophysical Research: Solid Earth*, *127*(11), e2022JB025117. https://doi.org/https://doi.org/10.1029/2022JB025117

Pease, A., Liu, J., Lv, M., Xiao, Y., Armstrong, K., Popov, D., et al. (2024). Strength, plasticity, and spin transition of Fe-N compounds in planetary cores. *Physics of the Earth and Planetary Interiors*, *355*, 107236. https://doi.org/10.1016/j.pepi.2024.107236

Pease, A., Liu, J., Lv, M., Piper, J., Kono, Y., & Dorfman, S. M. (2024, June). Dataset for "Liquid Structure of Iron and Iron- Nitrogen-Carbon Alloys within the Cores of Small Terrestrial Bodies." Zenodo. https://doi.org/10.5281/zenodo.12555446

Poirier, J.-P. (1994). Light elements in the Earth's outer core: A critical review. *Physics of the Earth and Planetary Interiors*, *85*(3), 319–337. https://doi.org/https://doi.org/10.1016/0031-9201(94)90120-1

Posner, E. S., & Steinle-Neumann, G. (2019). Mass Transport and Structural Properties of Binary Liquid Iron Alloys at High Pressure. *Geochemistry, Geophysics, Geosystems*, *20*(7), 3556–3568. https://doi.org/https://doi.org/10.1029/2019GC008393

Posner, E. S., Steinle-Neumann, G., Vlček, V., & Rubie, D. C. (2017). Structural changes and anomalous self-diffusion of oxygen in liquid iron at high pressure. *Geophysical Research Letters*, *44*(8), 3526–3534. https://doi.org/https://doi.org/10.1002/2017GL072926

Rubie, D. C., Jacobson, S. A., Morbidelli, A., O'Brien, D. P., Young, E. D., de Vries, J., et al. (2015). Accretion and differentiation of the terrestrial planets with implications for the compositions of early-formed Solar System bodies and accretion of water. *Icarus*, *248*, 89–108. https://doi.org/https://doi.org/10.1016/j.icarus.2014.10.015

Sanloup, C., Guyot, F., Gillet, P., Fiquet, G., Hemley, R., Mezouar, M., & Martinez, I. (2000). Structural changes in liquid Fe at high pressures and high temperatures from Synchrotron X-ray Diffraction. *Europhysics Letters*, *52*(2), 151. https://doi.org/10.1209/epl/i2000-00417-3

Sanloup, C., Guyot, F., Gillet, P., & Fei, Y. (2002). Physical properties of liquid Fe alloys at high pressure and their bearings on the nature of metallic planetary cores. *Journal of Geophysical Research: Solid Earth*, *107*(B11), ECV 4-1-ECV 4-9. https://doi.org/https://doi.org/10.1029/2001JB000808

Sanloup, C., Fiquet, G., Gregoryanz, E., Morard, G., & Mezouar, M. (2004). Effect of Si on liquid Fe compressibility: Implications for sound velocity in core materials. *Geophysical Research Letters*, *31*(7). https://doi.org/https://doi.org/10.1029/2004GL019526

Sanloup, C., van Westrenen, W., Dasgupta, R., Maynard-Casely, H., & Perrillat, J.-P. (2011). Compressibility change in iron-rich melt and implications for core formation models. *Earth and Planetary Science Letters*, *306*(1), 118–122. https://doi.org/https://doi.org/10.1016/j.epsl.2011.03.039

Schubert, G., Zhang, K., Kivelson, M. G., & Anderson, J. D. (1996). The magnetic field and internal structure of Ganymede. *Nature*, *384*(6609), 544–545. https://doi.org/10.1038/384544a0

Shen, G., Prakapenka, V. B., Rivers, M. L., & Sutton, S. R. (2004). Structure of Liquid Iron at Pressures up to 58 GPa. *Physical Review Letters*, *92*(18), 185701. https://doi.org/10.1103/PhysRevLett.92.185701

Shibazaki, Y., & Kono, Y. (2018). Effect of Silicon, Carbon, and Sulfur on Structure of Liquid Iron and Implications for Structure-Property Relations in Liquid Iron-Light Element Alloys. *Journal of Geophysical Research: Solid Earth*, *123*(6), 4697–4706. https://doi.org/https://doi.org/10.1029/2018JB015456

Shibazaki, Y., Kono, Y., & Fei, Y. (2015). Microscopic structural change in a liquid Fe-C alloy of ~5 GPa. *Geophysical Research Letters*, *42*(13), 5236–5242. https://doi.org/https://doi.org/10.1002/2015GL064271

Speelmanns, I. M., Schmidt, M. W., & Liebske, C. (2018). Nitrogen Solubility in Core Materials. *Geophysical Research Letters*, *45*(15), 7434–7443. https://doi.org/https://doi.org/10.1029/2018GL079130

Steenstra, E. S., Lin, Y., Rai, N., Jansen, M., & van Westrenen, W. (2017). Carbon as the dominant light element in the lunar core, *102*(1), 92–97. https://doi.org/doi:10.2138/am-2017-5727

Stevenson, D. J., Spohn, T., & Schubert, G. (1983). Magnetism and thermal evolution of the terrestrial planets. *Icarus*, *54*(3), 466–489. https://doi.org/https://doi.org/10.1016/0019-1035(83)90241-5

Terasaki, H., Nishida, K., Shibazaki, Y., Sakamaki, T., Suzuki, A., Ohtani, E., & Kikegawa, T. (2010). Density measurement of Fe3C liquid using X-ray absorption image up to 10 GPa and effect of light elements on compressibility of liquid iron. *Journal of Geophysical Research: Solid Earth*, *115*(B6). https://doi.org/https://doi.org/10.1029/2009JB006905

Trønnes, R. G., Baron, M. A., Eigenmann, K. R., Guren, M. G., Heyn, B. H., Løken, A., & Mohn, C. E. (2019). Core formation, mantle differentiation and core-mantle interaction within Earth and the terrestrial planets. *Tectonophysics*, *760*, 165–198. https://doi.org/https://doi.org/10.1016/j.tecto.2018.10.021

Tsuno, K., Grewal, D. S., & Dasgupta, R. (2018). Core-mantle fractionation of carbon in Earth and Mars: The effects of sulfur. *Geochimica et Cosmochimica Acta*, *238*, 477–495. https://doi.org/https://doi.org/10.1016/j.gca.2018.07.010

683 Umemoto, K., & Hirose, K. (2020). Chemical compositions of the outer core examined by first
684 principles calculations. *Earth and Planetary Science Letters*, *531*, 116009.
685 https://doi.org/https://doi.org/10.1016/j.epsl.2019.116009

686 Urakawa, S., Igawa, N., Kusaba, K., Olmo, H., & Shimomura, O. (1998). Structure of Molten Iron
687 Sulfide under Pressure. *Review of High Pressure Science and Technology/Koatsuryoku No*
688 *Kagaku To Gijutsu*, *7*, 286–288. https://doi.org/10.4131/jshpreview.7.286

689 Weber, R. C., Lin, P.-Y., Garnero, E. J., Williams, Q., & Lognonné, P. (2011). Seismic Detection of the
690 Lunar Core. *Science*, *331*(6015), 309–312. https://doi.org/10.1126/science.1199375

691 Zhang, Y., Sekine, T., He, H., Yu, Y., Liu, F., & Zhang, M. (2016). Experimental constraints on light
692 elements in the Earth's outer core. *Scientific Reports*, *6*(1), 22473.
693 https://doi.org/10.1038/srep22473

694 Zhao, B., Morard, G., Boulard, E., Boccato, S., Siersch, N. C., Rivoldini, A., et al. (2023). Local
695 Structure and Density of Liquid Fe-C-S Alloys at Moon's Core Conditions. *Journal of*
696 *Geophysical Research: Planets*, *128*(3), e2022JE007577.
697 https://doi.org/https://doi.org/10.1029/2022JE007577

698

699